Eur. Phys. J. B **26**, 273–289 (2002)
DOI: 10.1140/epjb/e20020090

THE EUROPEAN PHYSICAL JOURNAL B
EDP Sciences

Element-specific magnetic long- and short-range order and competing interactions in $Gd_xEu_{1-x}S$

D. Hupfeld[1], W. Schweika[1], J. Strempfer[2], W.A. Caliebe[1], U. Köbler[1], K. Mattenberger[3], G.J. McIntyre[4], F. Yakhou[5], and Th. Brückel[1,a]

[1] Institut für Festkörperphysik des Forschungszentrums Jülich, 52425 Jülich, Germany
[2] Northern Illinois University, Department of Physics, DeKalb, IL 60115, USA
[3] Labor für Festkörperphysik, ETH Hönggerberg, 8093 Zürich, Switzerland
[4] Institut Laue Langevin, BP 156, 38042 Grenoble Cedex 9, France
[5] European Synchrotron Radiation Facility ESRF, BP 220, 38043 Grenoble Cedex 9, France

Received 25 April 2001 and Received in final form 3 December 2001

Abstract. We report on an investigation of the magnetic properties of $Gd_xEu_{1-x}S$ mixed crystals with compositions in the range of $0.6 < x < 1$. For the two samples $Gd_{0.8}Eu_{0.2}S$ and $Gd_{0.73}Eu_{0.27}S$ a long-range antiferromagnetic order was observed at low temperatures. Element-specific measurements exhibited a different temperature dependence of the reduced sublattice magnetisation of the two magnetic species. A model calculation and Monte Carlo simulations revealed that the different temperature dependence is due to frustration effects. These frustration effects lead to a breakdown of the long-range order for higher europium contents. For the $Gd_{0.67}Eu_{0.33}S$-sample we were able to observe a short-range antiferromagnetic order with correlation lengths of a few 10 Å with X-ray resonance exchange scattering.

PACS. 75.25.+z Spin arrangements in magnetically ordered materials (including neutron and spin-polarised electron studies, synchrotron-source X-ray scattering, etc.). – 75.40.Cx Static properties (order parameter, static susceptibility, heat capacities, critical exponents, etc.) – 78.70.Ck X-ray scattering

1 Introduction

Since the first observation of a resonance enhancement at the L_{III}-edge of holmium in 1988 [1] many magnetic systems have been investigated with X-ray resonance exchange scattering (XRES) (see *e.g.* [2–7]). In contrast to the more traditional tools of magnetic neutron or non-resonant magnetic X-ray diffraction, XRES offers the unique possibility to distinguish the magnetic order of different elements in a magnetic alloy by tuning the X-ray energy to the absorption edges of the magnetic elements. Typically resonance enhancements of two orders of magnitude compared to non-resonant diffraction are obtained at the L_{II}- and L_{III}-edges of lanthanides. Therefore, if the photon energy is tuned to one of the L_{II}- or L_{III}-edges, the resonant scattering from the corresponding element largely dominates the non-resonant scattering from the other species. So far, all investigations of lanthanide mixed crystals (*e.g.* $Ho_{0.5}Er_{0.5}$ [8] or $Ho_{0.5}Tb_{0.5}$ [9]) revealed an identical temperature dependence of all magnetic species. It was argued that this would hold for all lanthanide systems, since the strong dipolar transitions involve the delocalised $5d$-states, while the magnetic moment is mainly due to the localised $4f$-states.

We investigated a highly disordered and frustrated system to observe the influence of frustration effects on the behaviour of the magnetic ions. An excellent example is given by mixed crystals of the series $Gd_xEu_{1-x}S$. While GdS is an antiferromagnetic metal, EuS is a ferromagnetic insulator. At intermediate concentrations of both elements in the mixed crystal $Gd_xEu_{1-x}S$, a low temperature spin glass phase exists [10].

We present in this paper element-specific measurements performed on a series of samples of $Gd_xEu_{1-x}S$ with x in the range of $0.6 < x < 1$. The samples cover the range where a long-range order of the magnetic ions exist to an intermediate regime with a spin glass phase [10]. We were able to observe a different behaviour of the two magnetic species in the antiferromagnetic (long-range) ordered regime. In the intermediate regime of x we were able to observe a short-range antiferromagnetic order. For the first time it was possible to observe antiferromagnetic order on a scale of about 40 Å with XRES.

We omit in this paper a description of XRES since it was discussed in detail by many authors [11–15]. For a short introduction we refer to our paper about an

[a] e-mail: T.Brueckel@fz-juelich.de

Table 1. Composition of the investigated samples determined with a microprobe (exact composition) as compared to the nominal composition from preparation. The error bars were calculated from the statistical scatter of the data and do not include systematic errors from calibration.

nominal composition	exact composition
$Gd_{0.8}Eu_{0.2}S$	$Gd_{0.782(5)}Eu_{0.187(5)}S_{1.031(5)}$
$Gd_{0.73}Eu_{0.27}S$	$Gd_{0.756(5)}Eu_{0.229(5)}S_{1.014(5)}$
$Gd_{0.67}Eu_{0.33}S$	$Gd_{0.664(5)}Eu_{0.305(5)}S_{1.030(5)}$
$Gd_{0.6}Eu_{0.4}S$	$Gd_{0.607(5)}Eu_{0.394(5)}S_{1.000(5)}$

investigation of GdS with XRES [16]. Some results for the $Gd_{0.8}Eu_{0.2}S$-sample have previously been published as a letter [17].

2 Experimental details

The synchrotron experiments described here were performed at the beamline W1 of the Hamburger Synchrotronstrahlungslabor (HASYLAB) at Deutsches Elektronensynchrotron (DESY). The beamline, which is located at the 4.5 GeV Doris III storage ring, operates with synchrotron light from a wiggler. It contains a fixed-exit Si(111) double-crystal monochromator and a focusing gold mirror. The band width of the monochromatic beam depends on the collimation of the white beam and lies in the range of 2–6 eV. In our case the energy resolution of the experiment is defined by the band width of the beamline, because the detector systems were used to determine the integral number of elastically scattered photons.

All samples used are single-crystals grown at the ETH Zürich by mineralisation [18]. They have dimensions of about $3 \times 3 \times 1$ mm^3. They were mounted in a liquid helium cryostat adapted for vertical scattering geometry at medium X-ray energies from 4 to 12 keV [19]. The characterisation of the $Gd_{0.8}Eu_{0.2}S$-sample was done with an X-ray microscope at HASYLAB [20]. No phase separation effects could be detected on a μm scale. In addition we searched for diffuse X-ray scattering employing anomalous scattering for contrast variation. No chemical short-range order could be detected. We conclude that our samples are homogeneous with a random occupation of the rare earth sites with Gd^{3+}– and Eu^{2+}-ions. The exact compositions of the samples were determined with a microprobe analysis as shown in Table 1. The composition is uniform over the whole sample.

Neutron scattering experiments were performed at the four-circle diffractometer D9 at a hot neutron beam of the Institut Laue Langevin (ILL) in Grenoble. A small two-dimensional position-sensitive detector was employed [21]. Neutrons of wavelength 0.47 Å obtained from a Cu(220) monochromator were used to reduce the strong absorption of natural gadolinium. An indium filter suppressed the $\lambda/2$ contribution. The $Gd_{0.8}Eu_{0.2}S$- and $Gd_{0.73}Eu_{0.27}S$-samples were mounted in a closed cycle cryostat with a base temperature of 14 K. For the investigation of the $Gd_{0.67}Eu_{0.33}S$-sample a liquid helium cryostat with a base temperature of 2 K was used.

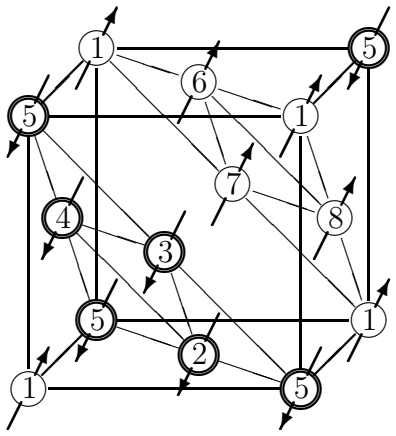

Fig. 1. The AF-II ordered structure. The numbers denote the eight simple cubic sublattices that are required to describe the AF-II type of order in general. Here we show a collinear spin structure alternating for subsequent layers in one of the ⟨111⟩ directions. (Note, the rule of opposite spins at next-nearest neighbour positions does not exclude more complicated canted ground states.)

3 Experimental results

In this chapter we present the results from measurements on four different samples of the series $Gd_xEu_{1-x}S$ with $x = 0.8$, 0.73, 0.67 and 0.6. The two samples $Gd_{0.8}Eu_{0.2}S$ and $Gd_{0.73}Eu_{0.27}S$ show a long-range order of the magnetic moments. For higher europium-contents in the $Gd_{0.67}Eu_{0.33}S$- and $Gd_{0.6}Eu_{0.4}S$-samples, the type II long-range order vanishes.

3.1 Long-range ordered state

Pure GdS exhibits antiferromagnetic order of the second type AF-II [16]. There are four possible domain orientations along the ⟨111⟩ directions and eight possible variants of this antiferromagnetic order, see Figure 1. Averaging over the intensities from the different domains related to these ordering variants leads to magnetic Bragg intensities at all reciprocal lattice positions of the type $\frac{1}{2}(n, n', n'')$, where n, n', n'' are odd integers. This is expected for samples with a sufficiently high gadolinium content.

First element-specific measurements with XRES at the $Gd_{0.8}Eu_{0.2}S$- and $Gd_{0.73}Eu_{0.27}S$-sample provided magnetic intensities at the $(\frac{1}{2}\frac{1}{2}\frac{9}{2})$-position, while the energy was tuned to the gadolinium-L_{II}- and -L_{III}-edges as well as to the europium-L_{II}- and -L_{III}-edges. From this follows that the europium-ions participate in the antiferromagnetic order of the gadolinium-ions.

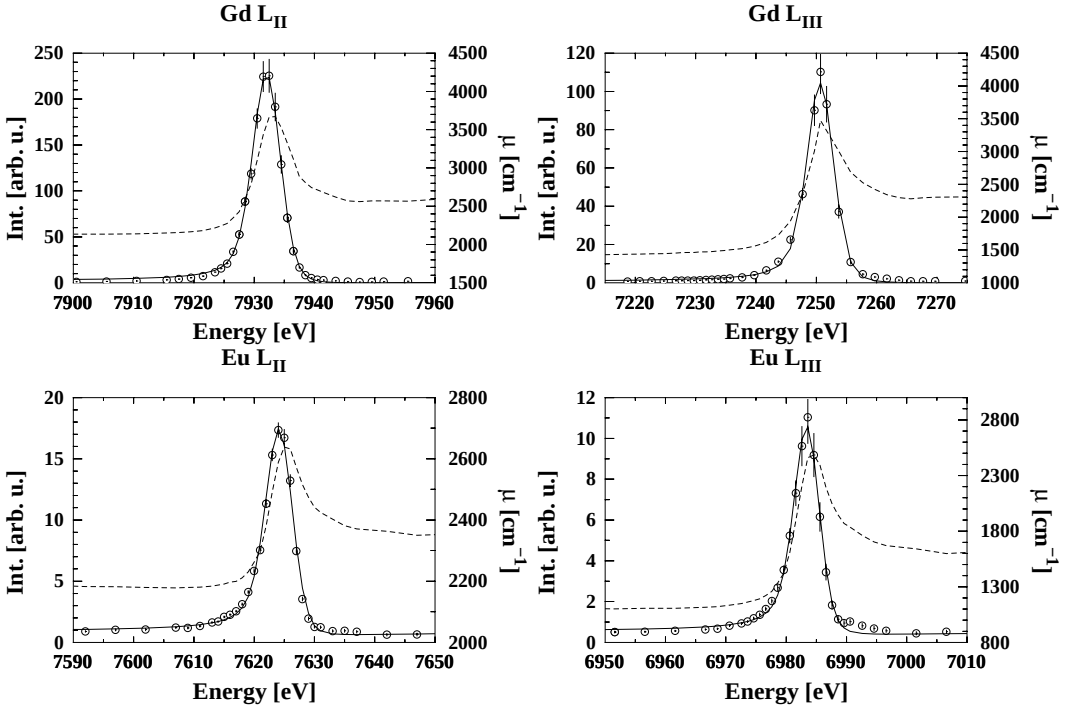

Fig. 2. Absorption corrected energy dependence of the intensity of the $(\frac{1}{2}\frac{1}{2}\frac{9}{2})$ magnetic Bragg-peak at the gadolinium- and europium-L_{II}- and -L_{III}-edges. The data were taken from the $Gd_{0.73}Eu_{0.27}S$-sample at 4 K. The solid lines represent a fit with equation (1) convoluted with the energy resolution of the beamline. The dashed line shows the energy dependence of the linear absorption coefficient μ in cm^{-1}, which we obtained from measurements of the fluorescence yield.

3.1.1 Energy dependence of XRES

To determine the energy dependence of XRES we performed measurements at the gadolinium- and the europium-L_{II}- and -L_{III}-edges. A germanium detector with an energy resolution of 250 eV was employed. This enabled us to separate the elastic signal and the fluorescence scattering to resolve the structure of the fluorescence lines. We used the energy dependence of the L_{β_1}-line at the L_{II}-edge and of the L_α-line at the L_{III}-edge to determine the energy dependence of the mass absorption coefficient as described in [16]. In Figure 2 the energy dependence of XRES is shown for the $Gd_{0.73}Eu_{0.27}S$-sample. Each datum point represents the integral intensity of a rocking curve measured at the specified energy. The data are corrected for absorption, following the procedure detailed in [16]. The absorption correction does not completely remove the asymmetry of the resonance line shape obtained in the raw data. The remaining asymmetry is caused by a superposition of XRES and non-resonant magnetic scattering. The resulting curve form is described by equation (1), which is derived in [16].

$$\frac{\mathrm{d}\sigma}{\mathrm{d}\Omega} \sim |A_M|^2 + \frac{|A_R|^2}{E^2}\frac{1}{(E-E_0)^2+\left(\frac{\Gamma}{2}\right)^2} + 2|A_M|\frac{|A_R|}{E}\frac{(E-E_0)}{(E-E_0)^2+\left(\frac{\Gamma}{2}\right)^2} \quad (1)$$

A_M and A_R are the amplitudes of the non-resonant magnetic scattering and XRES, respectively. Γ is the resonance level width and E_0 the resonance energy. The solid lines in Figure 2 represent a fit with equation (1) convoluted with the energy resolution of the monochromator (about 4 eV). The results of the refinement are given in Table 2. The resonance energy E_0 can be determined very accurately. However, the absolute energy calibration of the beamline is only feasible within a range of several eV. From the energy dependence of the fluorescence the energy of the absorption edge and of the white line can be determined. At all samples and measured edges the resonance energy coincides within the estimated standard deviation with the arithmetic mean between the energy of the absorption edge and the energy of the white line. In addition a simultaneous investigation of the energy dependence of the fluorescence of the different samples at the gadolinium and europium L_{II}- and L_{III}-edges showed that the absorption edge energy E_E and the energy of the white line E_{WL} agrees within the error bars for all samples. Therefore the absorption edge energy E_E has been normalised to values published in [22].

Due to the heat load on the monochromator, the energy resolution is not constant. This gives rise to systematic differences for measurements performed in different runs. The average level width is about 2.5 eV, corresponding to a core-hole lifetime of 0.26 fs. No difference between the resonance level width of the gadolinium- and europium-ions is observable.

Table 2. Spectroscopic data for the resonance behaviour of GdS, $Gd_{0.8}Eu_{0.2}S$, $Gd_{0.73}Eu_{0.27}S$ and $Gd_{0.67}Eu_{0.33}S$ at the $(\frac{1}{2}\frac{1}{2}\frac{9}{2})$ reflection at 4 K. The meaning of the symbols is as follows: E_E: Absorption edge energy (point of inflection) E_{WL}: White line energy (absorption maximum) E_0: Resonance energy (compare Eq. (1)) Γ: Resonance level width (compare Eq. (1)) $|A_R|^2, |A_M|^2$: Square of the amplitude of XRES and the non-resonant magnetic scattering, respectively (compare Eq. (1)). Values in parenthesis are estimated standard deviations due to counting statistics. In addition systematic errors have to be considered such as the uncertainty of the energy resolution (about 1 eV). Because no absolute energy calibration of the beamline was performed the absorption edge energy E_E was normalised to previously published values [22]. The energy of the white line E_{WL} and the resonance energy E_0 was corrected accordingly.

sample	edge	$\lvert A_R\rvert^2$	$\lvert A_M\rvert^2$	E_0/(eV)	E_E/(eV)	E_{WL}/(eV)	Γ/(eV)
GdS (Fig. 2 in [16])	$Gd_{L_{II}}$			7931.1(8)	7930	7932.0(1.4)	2.2(2)
	$Gd_{L_{III}}$			7245.0(5)	7243	7246.2(1.2)	2.8(2)
$Gd_{0.8}Eu_{0.2}S$ (Fig. 6.1 in [23])	$Gd_{L_{II}}$	460(16)	0.9(2)	7931.4(5)	7930	7933.9(1.0)	2.7(1)
	$Gd_{L_{III}}$	252(9)	0.6(1)	7246.0(5)	7243	7246.9(1.0)	2.9(1)
	$Eu_{L_{II}}$	21.4(1.3)	0.3(1)	7619.9(1.0)	7617	7621.5(2.0)	2.8(1)
	$Eu_{L_{III}}$	12.2(9)	0.1(1)	6979.4(5)	6977	6979.6(1.0)	2.8(1)
$Gd_{0.73}Eu_{0.27}S$ (Fig. 2)	$Gd_{L_{II}}$	588(32)	1.6(4)	7931.8(5)	7930	7933.1(1.0)	1.6(1)
	$Gd_{L_{III}}$	223(18)	0.5(2)	7245.6(5)	7243	7246.3(1.0)	1.9(1)
	$Eu_{L_{II}}$	42(4)	0.4(1)	7619.4(5)	7617	7620.6(1.0)	1.8(1)
	$Eu_{L_{III}}$	21(2)	0.1(1)	6979.0(5)	6977	6980.5(1.0)	1.9(1)
$Gd_{0.67}Eu_{0.33}S$ (Fig. 6)	$Gd_{L_{II}}$	1.67(13)	0	7930.8(8)	7930	7932.3(1.0)	3(2)

In the fourth column in Table 2 the non-resonant part $|A_M|^2$ of the magnetic scattering is listed. Because all of the data were corrected for absorption $|A_M|^2$ should be constant, which is not quite the case. The determination of the non-resonant magnetic scattering intensity is difficult because also very weak non-resonant non-magnetic scattering is observable. This is the reason for the large systematic errors of $|A_M|^2$. A comparison with datum points far away from the absorption edge shows that the order of magnitude of the intensity of the non-resonant magnetic scattering was determined correctly.

The magnitude of the resonance enhancement follows from the ratio of $|A_R|^2$ to $|A_M|^2$ and amounts to a factor of a few hundred with large standard deviations due to the uncertainty in $|A_M|^2$.

The branching ratio, the ratio between the absorption corrected maximum resonance intensity at the L_{II}- and L_{III}-edge, lies in the range from 1.8 to 2.6 and is comparable to 2.5 for GdS [16]. Within the estimated standard deviation (ESD) the branching ratios at the gadolinium- and europium-edges are identical.

A comparison of the element-specific intensities shows that for the $Gd_{0.8}Eu_{0.2}S$-sample for example the integral intensities measured at the gadolinium-edges are on average about a factor 21.4(2.2) larger than at the europium-edges. The stoichiometry of the sample has to be taken into account. The number ratio between gadolinium- and europium-ions is 4 : 1. This results in a 5.4(6) times larger scattering intensity at the gadolinium-edge as compared to the respective europium-edge. Taking the stoichiometry into account, factors of 5.2(8) and 3.9(7) have been determined for the L_{II}- and L_{III}-edges of the $Gd_{0.73}Eu_{0.27}S$-sample. Consistently for both samples the resonance enhancement at the gadolinium-edges is about a factor of five larger as at the europium-edges. For the study of the temperature dependence of the sublattice magnetisation, it is essential that the resonance line shape does not change with temperature. This has been checked for the $Gd_{0.8}Eu_{0.2}S$ sample with measurements at 4 K and 45 K, where no difference in line shape could be detected [23].

3.1.2 Temperature dependence of the reduced sublattice magnetisation

We have measured the temperature dependence of XRES at the gadolinium-L_{II}- and -L_{III}- and at the europium-L_{II}- and -L_{III}-edges. XRES, as a second order perturbation process [13], is not necessarily directly connected to the sublattice magnetisation (see however [14]). Therefore, we have performed additional neutron diffraction experiments to establish the relationship between the XRES intensity and the sublattice magnetisation. By a comparison between XRES and magnetic neutron scattering we could show in earlier experiments that for GdS the sublattice magnetisation is proportional to the square root of the integrated intensity of the magnetic Bragg reflections [16].

The investigation of the temperature dependence of the XRES of $Gd_{0.8}Eu_{0.2}S$ and $Gd_{0.73}Eu_{0.27}S$ revealed a completely different behaviour of the gadolinium- and europium-ions. In Figures 3 and 4, the square root of the integral intensity measured at the resonance energy at the L_{II}-edges of both elements, normalised to 1 for $T \to 0$, is plotted. We interpret this quantity as the element-specific reduced sublattice magnetisation of the Gd^{3+}- and Eu^{2+}-ions. To verify this assumption additional measurements

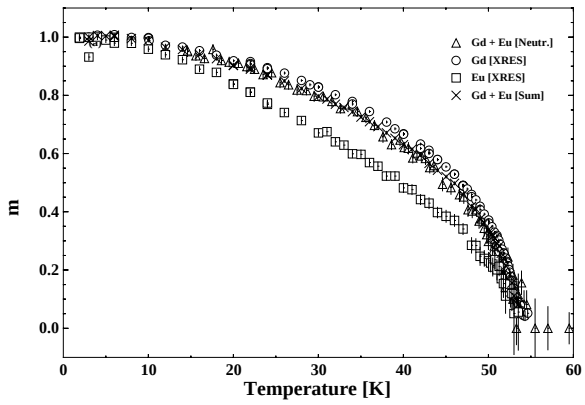

Fig. 3. Temperature dependence for the $Gd_{0.8}Eu_{0.2}S$-crystal. XRES has been used to determine separately the behaviour of the gadolinium- and europium-ions. With magnetic neutron scattering only the average magnetisation is accessible. For comparison with the neutron data the weighted sum, according to the stoichiometry, of the two XRES measurements is shown.

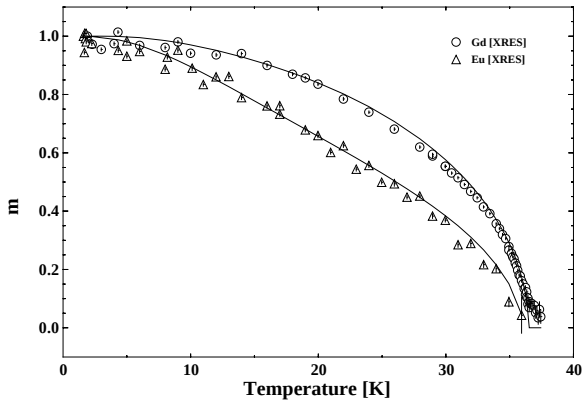

Fig. 4. Temperature dependence for the $Gd_{0.73}Eu_{0.27}S$-crystal. XRES has been used to determine separately the behaviour of the gadolinium- and europium-ions. The solid lines represent a fit to the data. For the Gd^{3+}-ions a mean field function for spin $S = \frac{7}{2}$ was used. The fit of the reduced sublattice magnetisation m of the europium-ions was done as described in the caption of Figure 7.

with magnetic neutron scattering have been performed for the $Gd_{0.8}Eu_{0.2}S$-sample. With magnetic neutron scattering only the average sublattice magnetisation is accessible. This average sublattice magnetisation and a weighted sum, according to the stoichiometry, of the two XRES measurements are compared in Figure 3. Both curves coincide within the error bars. This proves that the unusual temperature dependence of the XRES intensity of the europium-ions corresponds to an abnormal temperature dependence of their sublattice magnetisation. It also confirms that the europium-ions nearly reach the saturation magnetisation, a quantity not directly accessible by XRES. The insert in Figure 5 and the fit in Figure 4 clearly demonstrate that for both samples ($x = 0.8$ and $x = 0.73$), the sublattice magnetisation for the Gd^{3+}-ions follows perfectly a mean-field behaviour for $S = \frac{7}{2}$. This was also observed for pure GdS [16]. The temperature dependence of the reduced sublattice magnetisation of the europium-ions will be described by a mean-field model in Section 4 and a Monte Carlo Simulation (MCS) in Section 5.

In order to investigate the critical behaviour of the sublattice magnetisation for the $Gd_{0.8}Eu_{0.2}S$- and $Gd_{0.73}Eu_{0.27}S$-samples, we have taken many more data points with XRES in the critical region. Close to the Néel-temperature of both samples a broadening is observed indicating the presence of magnetic diffuse scattering. The statistical accuracy of our data was not high enough to perform a unique separation of the diffuse component. Therefore, data very close to the Néel-temperature had to be excluded from the determination of the critical exponent. Note, however, that due to the high Q-space resolution, T_N can nonetheless be approached quite closely before the diffuse component moves into the resolution window of the experiment. In Figure 5 the remaining data of the reduced sublattice magnetisation of the gadolinium-ions is shown in a double logarithmic plot. The straight line corresponds to a critical exponent which is defined as

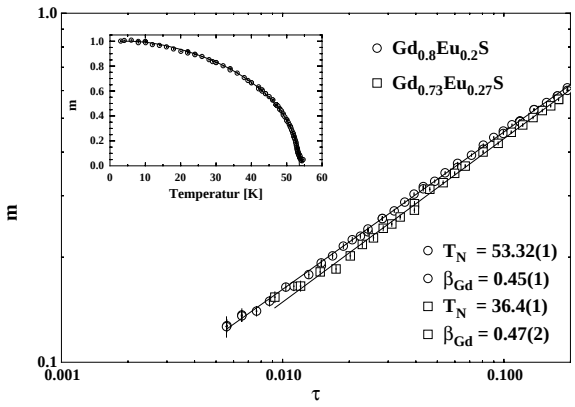

Fig. 5. Temperature dependence of the reduced sublattice magnetisation *versus* the reduced temperature τ of the Gd^{3+}-ions for the $Gd_{0.8}Eu_{0.2}S$- and $Gd_{0.73}Eu_{0.27}S$-samples. The inset shows a fit with a mean field function for spin $S = \frac{7}{2}$ to the reduced sublattice magnetisation of $Gd_{0.8}Eu_{0.2}S$. For the $Gd_{0.73}Eu_{0.27}S$-sample the fit is shown in Figure 4.

follows:

$$m \sim \tau^{\beta_{\mathrm{Gd}}}, \quad \text{with} \quad \tau = \frac{T_{\mathrm{N}} - T}{T_{\mathrm{N}}} \quad \text{and} \quad m = \frac{M}{M_{\mathrm{s}}} \cdot \quad (2)$$

Here M, M_{s} and T_{N} denote the sublattice magnetisation, the saturation value of the sublattice magnetisation and the Néel-temperature, respectively. The critical exponents β_{Gd} and Néel-temperatures determined for the different samples are listed in Table 3. For a comparison the values for pure GdS are also listed [16,24]. The paramagnetic Curie-Weiss temperature was determined with magnetisation measurements using a Faraday balance [25]. The coupling constants J_1 and J_2 have been calculated

Table 3. Néel-temperatures, paramagnetic Curie-Weiss temperatures, critical exponents β_{Gd} for the gadolinium-subsystem and coupling constants J_1 for nearest neighbour and J_2 for next nearest neighbour interactions as determined for GdS, $Gd_{0.8}Eu_{0.2}S$ and $Gd_{0.73}Eu_{0.27}S$. Below the temperature labelled with * a short-range antiferromagnetic order was observable for the $Gd_{0.67}Eu_{0.33}S$-sample (see Sect. 3.2). The coupling constants for the mixed crystals represent the average of the coupling constants of the gadolinium- and europium-ions which cannot been determined separately from the Néel- and Curie-Weiss temperatures.

Sample	T_{N}/ K	Θ_c/ K	β_{Gd}	J_1/ K	J_2/ K
GdS[16]	57.72(3)	−110 [24]	0.378(20)	−0.42	−0.92
$Gd_{0.8}Eu_{0.2}S$	53.32(1)	−61 [25]	0.45(1)	−0.03	−0.91
$Gd_{0.73}Eu_{0.27}S$	36.4(1)		0.47(2)		−0.59
$Gd_{0.67}Eu_{0.33}S$	23(2)*	−32 [25]			

from T_{N} and Θ_c using the following equations [26]:

$$k_{\mathrm{B}}T_{\mathrm{N}} = \frac{2}{3}S(S+1)(-6J_2) \tag{3}$$

$$k_{\mathrm{B}}\Theta_c = \frac{2}{3}S(S+1)(12J_1+6J_2) \tag{4}$$

J_1 and J_2 are also shown in Table 3. The statistic of the reduced sublattice magnetisation of the europium-ions is not good enough to determine a critical exponent β_{Eu}.

3.2 Short-range ordered state

In contrast to the samples with higher gadolinium concentration, for the $x = 0.67$ sample we could not find magnetic Bragg peaks corresponding to a type II antiferromagnetic order. By means of XRES as well as hot neutron diffraction, we searched the reciprocal space for reflections corresponding to antiferromagnetic order of type I, II and III. None of these scans nor scans along all main cubic symmetry directions revealed any long-range antiferromagnetic order. According to the phase diagram of the $Gd_xEu_{1-x}S$ mixed crystals proposed in [10], the transition to a spin-glass state occurs for $x < 0.6$. Short-range antiferromagnetic correlations will lead to broad structures with very low peak intensities. Therefore we employed a pyrolytic graphite crystal as polarisation analyser in $\sigma \rightarrow \pi$ geometry. The background caused by non-magnetic charge scattering is largely suppressed since for charge scattering the polarisation is not rotated. With this method we were able to detect magnetic diffuse scattering at the $(\frac{1}{2}\frac{1}{2}\frac{9}{2})$-position in resonance at the $Gd_{L_{II}}$-edge at 4 K. In Figure 6 a scan in reciprocal space from $Q = (0.3\ 0.3\ 4.3)$ to $Q = (0.7\ 0.7\ 4.7)$ around the $(\frac{1}{2}\frac{1}{2}\frac{9}{2})$-position is shown. We observed a peak intensity of 0.6 photons/s above a background of 1.5 photons/s which leads to a peak to background ratio of 0.4 : 1. To improve the statistics of the experiment we repeated this measurement at the beamline ID-20 at the ESRF. We gained a factor 6 in intensity, the peak to background ratio was determined to be 0.7 : 1.

From the full width at half maximum (FWHM) of the magnetic diffuse scattering the correlation length can be determined. The instrumental resolution is about three orders of magnitude better compared to the FWHM and can be neglected. The correlation length was determined from the reciprocal lattice units (r.l.u.) with the following equation:

$$\xi = \frac{a_0}{\sqrt{\Delta h^2 + \Delta k^2 + \Delta l^2}}\,. \tag{5}$$

Here a_0 denotes the lattice constant and Δh, Δk and Δl the FWHM in $\langle hkl\rangle$-direction, respectively. At 4 K the $Gd_{0.67}Eu_{0.33}S$-sample has a lattice constant of $a_0 = 5.66$ Å. From the measurement at the $(\frac{1}{2}\frac{1}{2}\frac{9}{2})$-position shown in Figure 6, a correlation length of 35(4) Å was calculated. Q-scans in the $\langle 001\rangle$-, $\langle 110\rangle$- and $\langle 111\rangle$-directions performed at beamline ID-20 at the ESRF lead to correlation lengths of 46(4) Å, 37(3) Å and 56(4) Å, respectively.

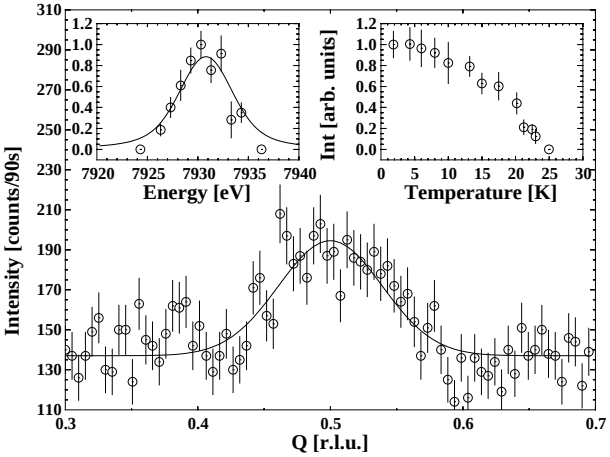

Fig. 6. $Gd_{0.67}Eu_{0.33}S$ Q-scan $(0.3\ 0.3\ 4.3) \longrightarrow (0.7\ 0.7\ 4.7)$ around the $(\frac{1}{2}\frac{1}{2}\frac{9}{2})$-position. The counting time was 90 seconds for each datum point. The energy was tuned to the gadolinium L_{II}-edge; the temperature was 4 K. A polarisation analyser with $\sigma \longrightarrow \pi$ geometry was used. The solid line represents the fit of a Gaussian curve to determine the integrated intensity. The left inset shows the energy dependence of the magnetic scattering around the $(\frac{1}{2}\frac{1}{2}\frac{9}{2})$-position at the gadolinium-L_{II}-edge. The right inset shows the temperature dependence of the magnetic scattering around the $(\frac{1}{2}\frac{1}{2}\frac{9}{2})$-position in resonance at the gadolinium-L_{II}-edge.

Measurements at the $Eu_{L_{II}}$-edge at the ESRF did not reveal magnetic intensities, neither Bragg nor diffuse scattering. Taking into consideration the factor five between the resonance enhancement at the gadolinium-L_{II}-edge compared to the europium-L_{II}-edge, the statistical accuracy of our measurements would have been good enough to detect antiferromagnetic correlations of europium-ions down to 20 Å correlation length. We conclude that within these limits the europium-ions do not participate in the antiferromagnetic short-range ordering. A short-range ferromagnetic order of the europium-ions cannot be investigated with our method, because the magnetic scattering intensity occurs at the same position as the charge scattering which is about 10 orders of magnitude larger.

We also investigated the energy dependence of XRES at the $Gd_{L_{II}}$-edge of the $Gd_{0.67}Eu_{0.33}S$-sample as shown in the left inset of Figure 6. The parameters determined with a fit of equation (1) are also shown in Table 2. They are comparable to the values determined for the long-range antiferromagnetically ordered systems $Gd_{0.8}Eu_{0.2}S$ and $Gd_{0.73}Eu_{0.27}S$. The temperature dependence of the integrated intensity is shown in the right inset of Figure 6. Magnetic diffuse scattering can be observed up to 23(2) K. Please note that the temperature dependence of the integrated intensity is shown and not the temperature dependence of the reduced sublattice magnetisation which is identified with the square root of the integrated intensity for long-range ordered systems.

Note that due to the high absorption cross section of gadolinium and europium, we were not able to measure the short-range correlations by means of neutron diffraction, despite the fact that the momentum-space resolution is much better adapted.

An investigation of a $Gd_{0.6}Eu_{0.4}S$-crystal with XRES was performed employing the same method as for the $Gd_{0.67}Eu_{0.33}S$-sample described above. Comparative measurements at the charge reflections revealed the same scattering intensities and quality of the crystals as for the $Gd_{0.67}Eu_{0.33}S$-sample. We were not able to observe any magnetic diffuse scattering at the $(\frac{1}{2}\frac{1}{2}\frac{9}{2})$-position.

4 Mean-field model

The europium-ions in the $Gd_{0.8}Eu_{0.2}S$- and $Gd_{0.73}Eu_{0.27}S$-mixed-crystals participate in the antiferromagnetic ordering of the gadolinium subsystem. As expected for a collective phase transition, the long-range order of the europium and gadolinium subsystem sets in at the same Néel-temperature. However, the europium subsystem exhibits a completely different temperature dependence of the reduced sublattice magnetisation, see Figures 3 and 4. As was verified with neutron measurements at the $Gd_{0.8}Eu_{0.2}S$-sample (compare Fig. 3) the different temperature dependences of the europium- and gadolinium-ions are not caused by methodical or experimental reasons.

To come to an understanding of the unusual temperature dependence, we have performed model calculations as detailed in Appendix A. In the fcc-structure of

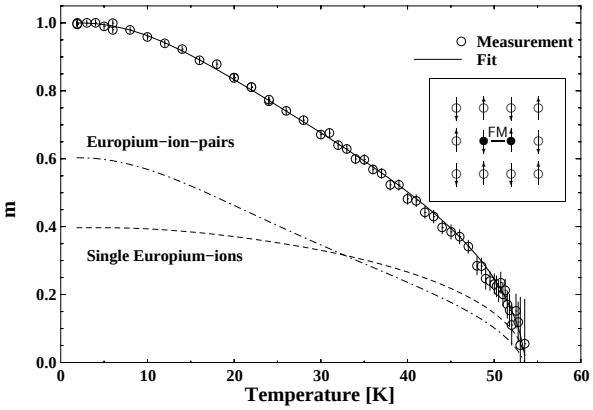

Fig. 7. Fit of the reduced sublattice magnetisation m of the europium-ions of the $Gd_{0.8}Eu_{0.2}S$-sample with a combination of a MF theory, representing the behaviour of single europium-ions, and a so called "frustrated" MF theory, representing the behaviour of europium-ion-pairs. The two curves were weighted with the statistical likelihood of single europium-ions and europium-ion-pairs. Larger europium-clusters were neglected. The insert demonstrates schematically the frustration effect for a ferromagnetic (FM) coupled Eu^{2+}-pair in the antiferromagnetic Gd^{3+}-environment.

$Gd_xEu_{1-x}S$ the nearest neighbour interaction is topologically frustrated. Therefore, next nearest neighbour interactions have to be taken into account. Moreover, in the metallic phase the dominant interaction is of RKKY-type, which is long ranged. In order to avoid all complications due to a large parameter space and to catch the main physical effect, we have chosen the most simple model system possible, for which the observed effect can be expected. In the model presented in Appendix A, we assume that the Gd- and Eu-ions are distributed randomly on a simple cubic lattice and interact with nearest neighbour exchange only. To obtain the correct type of magnetic order for the endmembers, we assume that the Eu-Eu exchange is ferromagnetic, while the Gd-Gd exchange is antiferromagnetic. For small Eu concentrations, we treat the Gd subsystem in a mean field (MF) approximation, while the Hamiltonian for Eu clusters in the Gd matrix is solved exactly. Frustration arises in Eu-pairs due to the ferromagnetic coupling of the Eu-ions, while the coupling to the neighbouring Gd ions is antiferromagnetic (see insert in Fig. 7). Our model calculations show that the anomalous temperature dependence of the europium subsystem is due to this frustration effect. Single europium-ions, which have only gadolinium-ions as nearest neighbours, participate in the antiferromagnetic ordering of the gadolinium-ions and exhibit the same mean-field behaviour (Eq. (19)). The behaviour of europium-pairs can be described by a "frustrated" mean-field curve (Eq. (27)).

To test the model proposed in Appendix A we first calculated the behaviour of gadolinium-ions in a gadolinium-surrounding. The result was a mean-field like curve as expected. The parameters used are listed in Table 4 in the column gadolinium-pairs. In Figures 7 and 4 the fits of the reduced sublattice magnetisation of the europium-ions of

Table 4. Parameters used during the fit of a "frustrated" Brillouin-function to the temperature dependence of the reduced sublattice magnetisation. J_{GG}, J_{EE} and J_{EG} are the coupling constants between Gd-Gd-, Gd-Eu- and Eu-Eu-pairs, respectively. Note that the calculations have been done on a simple cubic lattice for nearest neighbour exchange interactions only and that the parameters obtained cannot be interpreted as the true exchange interactions for the $Gd_xEu_{1-x}S$ system.

sample	gadolinium-pairs J_{GG} / K	europium-pairs J_{EE} / K	J_{EG} / K
GdS	−1.03		
$Gd_{0.8}Eu_{0.2}S$	−0.95	+0.70	−0.59
$Gd_{0.73}Eu_{0.27}S$	−0.60	+0.69	−0.41

the $Gd_{0.8}Eu_{0.2}S$- and $Gd_{0.73}Eu_{0.27}S$-samples are shown, respectively. Also included in Figure 7 is a plot of the behaviours of single europium-ions and europium-ion-pairs weighted with their stochastical probability. The parameters used for the "frustrated" Brillouin-function are shown in Table 4 in the columns europium-pairs.

The temperature dependence of the reduced sublattice magnetisation of the $Gd_{0.8}Eu_{0.2}S$- and $Gd_{0.73}Eu_{0.27}S$-samples can be described with the model calculations detailed in Appendix A. The crude simplifications of a simple cubic lattice with nearest neighbour interactions only and the neglect of the retroaction of the europium-pairs on the surrounding atoms do not allow us to determine the exchange parameters quantitatively. This explains the difference between the values in Table 3 and Table 4. However, despite its simplicity, the model shows that competing exchange interactions and frustration effects are the reason for the anomalous temperature dependence of the reduced sublattice magnetisation of the europium-ions in the $Gd_{0.8}Eu_{0.2}S$- and $Gd_{0.73}Eu_{0.27}S$-samples.

5 Monte Carlo simulations

In order to explore the frustration effects and observed changes in the critical behaviour in more detail, Monte Carlo simulations (MCS) have been performed using a Hamiltonian for a $S = \frac{7}{2}$ spin model

$$\mathcal{H} = -\sum_{i,j} J_{ij} \mathbf{S}_i \cdot \mathbf{S}_j \,, \tag{6}$$

where J_{ij} is the effective exchange interaction between spins at lattice sites i and j. In this semi-classical model the axis of quantisation was chosen arbitrarily parallel to the z direction, with $S_z = -\frac{7}{2}, ..., \frac{7}{2}$, S_x and S_y having continuous degrees of freedom and $|S| = \sqrt{\frac{7}{2}(\frac{7}{2}+1)}$. For comparison some results have been obtained from calculations based on a classical Heisenberg model with equivalent exchange interactions. For the MCS we used a tentatively more realistic interaction model (in comparison to the MF treatment) extending to second nearest neighbours on the fcc-cation-sublattice, see Table 5. Different to the model given in Table 4 these parameters are chosen independently of the composition. The interactions have been estimated from the Néel-temperatures and from the paramagnetic Curie-Weiss temperatures, however, these interaction parameters for the MC simulation are about 1.5 times larger than the original MF-estimates. All calculations are done at zero field.

Table 5. Effective interactions used in the Monte Carlo simulations.

	GdGd	GdEu	EuEu
J_1	−1.27 K	−0.85 K	+1.21 K
J_2	−2.82 K	−1.86 K	0

We used models with periodic boundary conditions with sizes ranging from a few hundred to about 35 000 atoms; after relaxation, thermal averages have been taken for (up to) 50 000 Monte Carlo steps/site.

Averages were taken to characterise the order, higher order cumulants of the order parameter, the pair correlations between nearest and second nearest neighbouring spins $\langle \mathbf{S}_i \cdot \mathbf{S}_j \rangle$, and, in more detail, the distribution of angles between these spins. All these quantities have been distinguished with respect to the specific elements.

The order parameter $\mathbf{m}_l$ of the variants l of the AF-II type of order, see Figure 1, can be defined as

$$\mathbf{m}_l = \frac{1}{8} \sum_j \langle \mathbf{S}_j \rangle \, \mathrm{e}^{2\pi \mathrm{i}\, \mathbf{h}_l \cdot \mathbf{x}_j} \,/\, |\mathbf{S}| \,, \tag{7}$$

where $\mathbf{h}_l$ is a member of the ordering star $\mathbf{h}^* = \frac{1}{2}\langle 111 \rangle$, $\langle \mathbf{S}_j \rangle$ is the magnetisation of the sublattice j; the order parameters $\mathbf{m}_l$ are normalised by $|\mathbf{S}|$.

One can distinguish four possible domain orientations along the $\langle 111 \rangle$ directions, eight possible variants of antiferromagnetic order, and eight different sublattices. The ground state properties and the high degeneracy of the AF-II type of order have been analysed in [27].

Note that the order parameters $\mathbf{m}_l$ are not scalar quantities. During the "observation time" in the MCS the order parameters may turn in space and also in the higher dimensional space of the order parameter components different linear combinations will occur. Therefore – for the whole system as well as for the specific elements – a positive definite total order parameter m, which includes all possible variants $\mathbf{m}_l$ is more appropriate to use

$$m = \left(\sum_l \mathbf{m}_l^2 \right)^{1/2} . \tag{8}$$

Figure 8 shows the results for the order parameters m, m_{Gd} and m_{Eu}. While – as expected for such a classical calculation – the slope at low temperatures deviates from our experimental data, at higher temperatures the frustration effects as seen in the MF treatment can be confirmed. Note, that the MF-results have to be taken with some

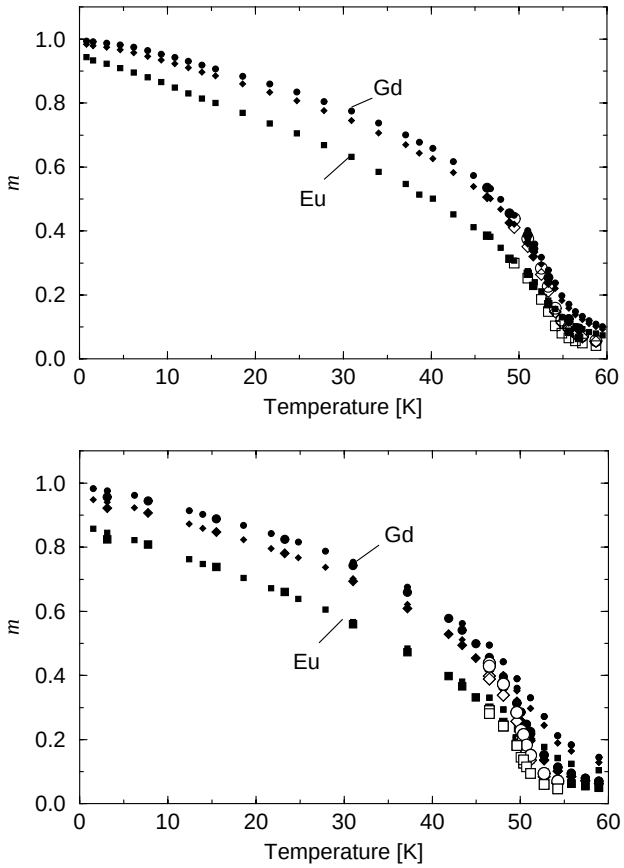

Fig. 8. Element-specific order in MCS. Temperature dependence of the order parameter m; top: $x = 0.8$, bottom: $x = 0.73$. (The symbol size is related to the different model sizes.)

caution; one cannot expect that MF theory predicts the correct critical temperature, in particular for a frustrated system. Typically, MF approximations overestimate T_N by a factor comparable to the critical exponent γ. However, the overall shape of the curve $m(\tau)$ can be well reproduced by our improved MF model.

5.1 Frustration effects

From the averages for the angles between spins for first and second neighbours it is found that (in the MCS) the Eu-Eu spin pairs between second neighbours do not follow the ideal collinear AF structure even at very low temperature. In view of the result from the MCS that m_{Eu} is little but significantly less than 1 for the ground state at $T = 0$, a similar behaviour in the real system is plausible and likely. This is not at variance to the experimental results because an absolute calibration cannot be made with sufficient accuracy.

The distributions of spin correlations of configurations at various temperatures have been analysed; they are shown in Figure 9. There is a fine-structure due to the discrete levels of S_z. In particular at high temperatures it resembles the spectrum for a random configuration of spins with $S_z = -\frac{7}{2}, ..., \frac{7}{2}$. Apart from this fine-structure at higher temperatures the angular distribution becomes rather broad and there are no specific perpendicular spin orientations, neither for Eu-Eu nor for Eu-Gd neighbours in our model.

The first neighbour correlations $\langle \mathbf{S}_i \cdot \mathbf{S}_j \rangle$ are completely frustrated for the AF-II structure. Therefore, the correlations in particular between the majority spins, the Gd-pairs, average to zero, although the distribution has detailed structures due to the discrete levels of S_z and the distribution also depends upon temperature and Eu-content.

The Eu-spins introduce with increasing concentration more and more competing interactions. There is a noteworthy effect on the correlation between Gd-Gd pairs, which becomes especially transparent in simulations using a classical Heisenberg-spin model. Considering first the pure GdS model, we find at high temperatures a random spin correlation distribution where $N(\alpha) \propto \sin\alpha$, and that lowering the temperature leads to more and more collinear spin configurations and finally to the collinear AF-II ground state. Recall, that the AF-II structure is essentially determined by second nearest neighbour interactions, leading to an AF-ordering on the four simple cubic (*sc*) sublattices of the *fcc* cation sublattice. In absence of any nearest neighbour interaction (or any longer ranged couplings between the four *sc* sublattices) the AF-orderings on the four *sc* sublattices are independent of each other and in general non-collinear. Collinear ordering of the AF-II type of order occurs, however, in case of pure systems (independent of the sign of the bilinear coupling), apparently because there is a higher density of excited states at low energies for the collinear state as compared to canted states.

For temperatures below T_N, we observed in our simulations that with increasing Eu content angles near to 90 degrees occur with higher probability while the weakly perturbed GdS shows a double peak distribution with a local minimum at 90 degrees. One may note that these frustrations effects are similar to that what would be expected from terms of biquadratic exchange (which are not present in our model).

A particularly intriguing result of the MCS is that with additional contents of Eu the nearest neighbour correlations between Gd spins are more in favour of canted states instead of collinear states as shown in Figure 10. At very low temperatures the broad maximum at 90 degrees splits into two or even more peaks depending on the composition. This is consistently found for initially ordered and disordered start configurations. The simulations indicate that competing interactions inferred by the minority atoms ("Eu") lead to non-collinear nearest neighbour pairs also of the majority atoms ("Gd"), and the formation of canted ordered states, in which the AF order is still preserved. We have not yet explored the variety of possible ordered states, which will be a difficult problem. No threshold concentration could be determined so far. In the simulations an increasing number of ordered states with different canting angles appeared. Considerably more

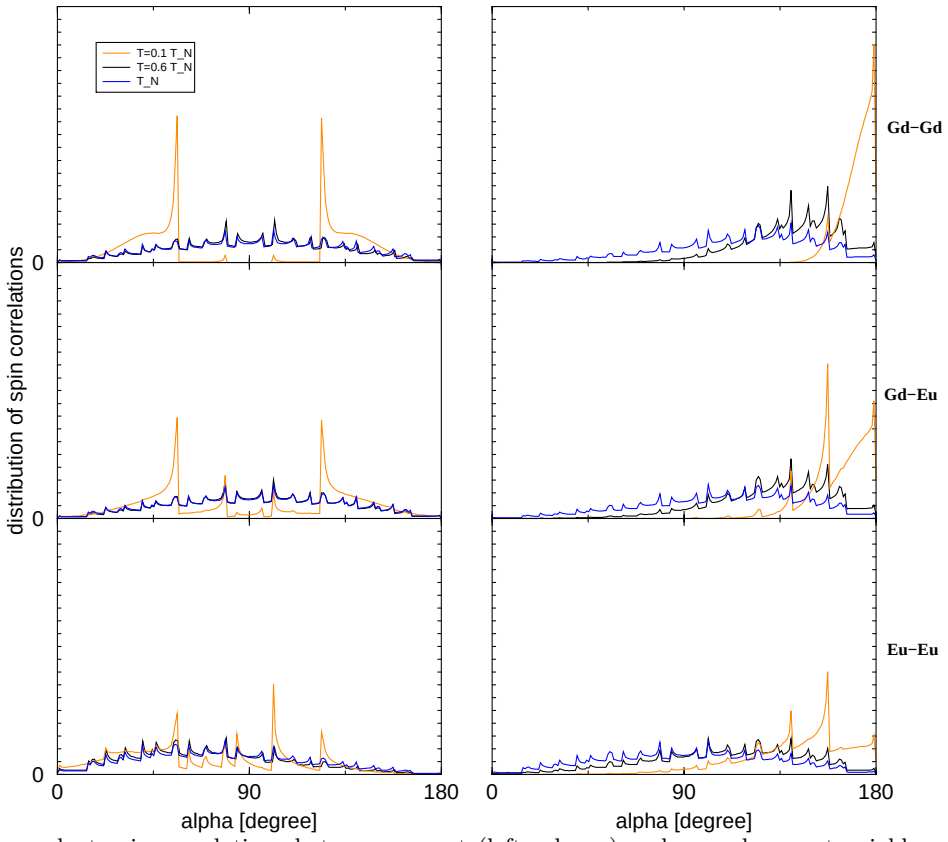

Fig. 9. Species dependent spin correlations between nearest (left column) and second nearest neighbours (right column) in $S = 7/2$ models of $Gd_{0.8}Eu_{0.2}S$ for different temperatures, $T/T_N = 0.1$, 0.6, 1.

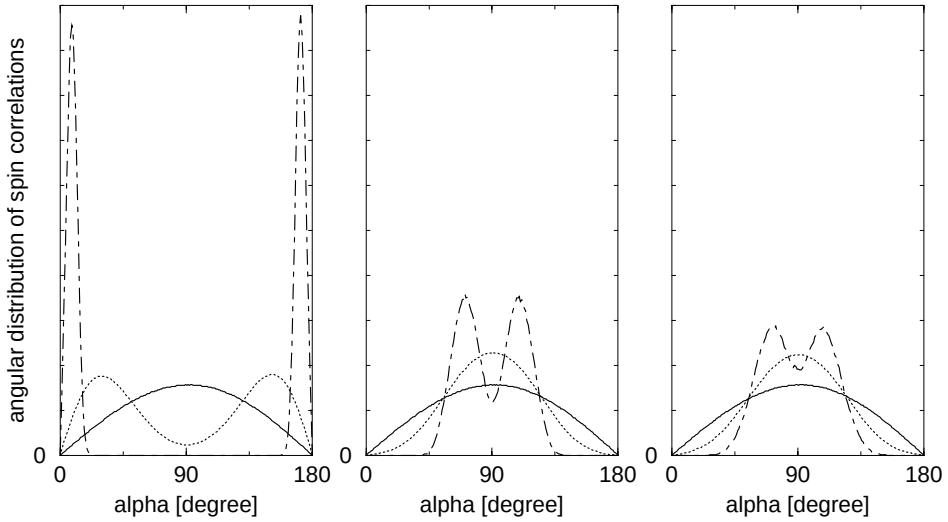

Fig. 10. Spin correlations between nearest neighbours in classical Heisenberg models of GdS, $Gd_{0.8}Eu_{0.2}S$ and $Gd_{0.73}Eu_{0.27}S$ (from left to right) for different temperatures, $T/T_N \approx 0.02$, 0.25, ∞ (dashed-dotted, dotted and solid lines, respectively). Note that in the high temperature limit $N(\alpha) \propto \sin\alpha$ resembles the density of possible states.

effort is needed to analyse their stability and determine the phase diagram.

Since in the first Born approximation the scattering intensity is related to pair-correlations only, this cannot provide a direct observation of the distribution of spin correlations in such frustrated magnets. The intensity variation when applying an external field could allow to discriminate between collinear and canted ordered states.

There is another noteworthy observation. Analysing the ordered states, both *collinear* and *non-collinear* configurations, we could not find domain walls in our models, – which at first was also not expected because of the small size of the models –, however, in general, different ordering variants contributed to the total order parameter of the models, even for highly ordered configurations with $m \approx 1$. Figure 11 illustrates the non-collinear sublattice

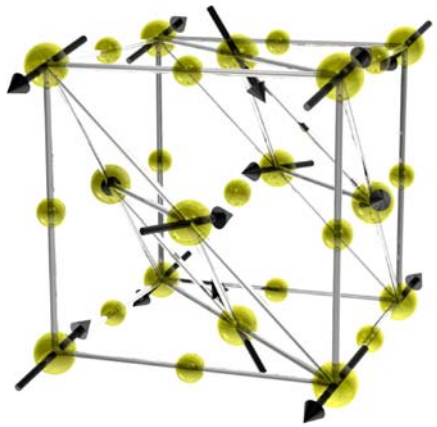

Fig. 11. Canted ordered AF-II structure found in MCS for $Gd_{0.8}Eu_{0.2}S$. For a comparison with a not canted structure see Figure 1.

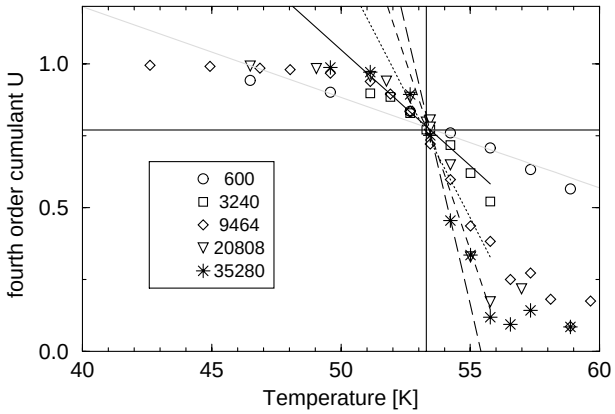

Fig. 12. Fourth order cumulant of the total order parameter m plotted *vs.* temperature for five different system sizes of models with $x = 0.8$. The crossing determines $T_N = 53.3(2)$ K and $\tilde{U}^* = 0.77(2)$.

magnetisations of one of the canted ordered states found in the simulation. An explanation for the absence of domain walls is that the individual spins have non-vanishing contributions to more than one of the different ordering variants $\mathbf{m}_l$. This peculiar behaviour has been previously observed in "multiple q" modulated magnetic structures; the non-collinear ordering in Nd [28] is such an example.

5.2 Critical behaviour

The distribution of the spin orientations changes upon ordering from a Gaussian distribution at high temperatures to a distribution that is peaked in response to the number of independent ordering variants. Therefore, the higher moments of the spin distribution are of interest in Monte Carlo studies of phase transitions. In particular, Binder [29] has shown that the 4th-order cumulants depend on T and lattice size L but cross at the critical temperature, where the fix-point $\tilde{U}(T, L)$ is a universal quantity. In the analysis of the MCS we use this property to determine the critical temperature. Note, that in the power-law fit to the experimental data correlations between the critical exponent β and the critical temperature cannot be avoided. Here we used the 4th-order cumulant

$$\tilde{U} = 7 - 6\frac{\langle m_t^4 \rangle}{\langle m_t^2 \rangle^2} \tag{9}$$

with the properties that at $T = 0$, $\langle m^4 \rangle = \langle m^2 \rangle = 1$ and therefore $\tilde{U} = 1$ and for $T \gg T_c$ the cumulant tends to zero.

In principle, the exponent ν can be determined independently from the slope

$$\left.\frac{\partial \tilde{U}_{L'}}{\partial \tilde{U}_L}\right|_{\tilde{U}^*} = \left\{\frac{L'}{L}\right\}^{1/\nu} . \tag{10}$$

However, the determination of this derivative with sufficient numerical accuracy requires extreme efforts and is not precise enough for the presently available Monte Carlo results.

According to the theory of finite size scaling [29,30], if the dependence of a physical quantity Q of a thermodynamic system on the parameter τ, which vanishes at the critical point $\tau = 0$, is of the form $Q \propto |\tau^a|$ near the critical point, then for a finite system of linear dimension L, the corresponding quantity $Q(L, \tau)$ is of the form:

$$Q(L, \tau) \approx L^{ay_t} F(\tau L^{y_t}) , \tag{11}$$

where $y_t = 1/\nu$ is the thermal scaling power and $F(x)$ is the finite size scaling function. It follows from (11) that the scaled data $Q(L, \tau)L^{ay_t}$ for different values of L and τ can be described as a single function of the scaling variable $x = \tau L^{y_t}$. Hence, one obtains the scaling expression for the order parameter

$$m(L, \tau) \approx L^{-\beta/\nu} F(\tau L^{1/\nu}) , \tag{12}$$

which can be used to determine the critical exponents β and ν. Recall that T_N follows independently from the behaviour of the cumulant $\tilde{U}(T, L)$.

For the analysis of the finite size effects we distinguished the thermal avarages of m, m_{Gd} and m_{Eu} and their fourth order cumulants. First, we consider the $S = 7/2$ model for $Gd_{0.8}Eu_{0.2}S$. Figure 12 illustrates the determination of the critical temperature from the cumulant crossing method.

A data collapse is found in the finite size scaling plot of the total order parameter but also of the element-specific order parameters using critical exponents close to the Heisenberg values, see Figure 13.

Based on the same interaction-model we also studied models of the more frustrated system $Gd_{0.73}Eu_{0.27}S$ and the pure system GdS. Figure 14 shows the determination of T_N for the model of $Gd_{0.73}Eu_{0.27}S$. In the MCS the critical exponents are not significantly altered with increasing content of ferromagnetic impurities as can be seen in the finite size scaling plots shown in Figure 15.

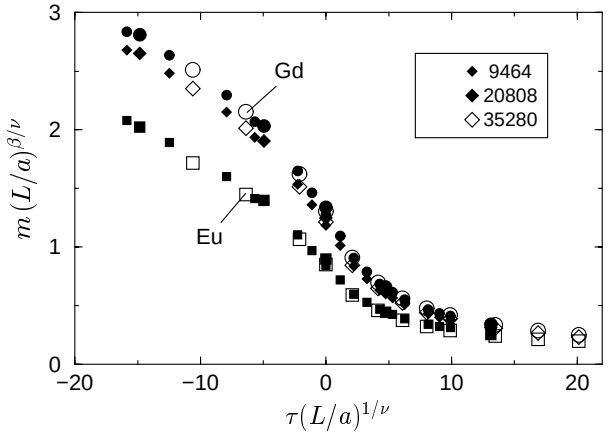

Fig. 13. Finite size scaling plot of the order parameter m and of the element-specific order parameters for the composition $x = 0.8$ with $T_{\rm N} = 53.3$ K, $\nu = 0.7$ and $\beta = 0.35$ (five different system sizes are shown; circles (squares) represent the Gd (Eu) order).

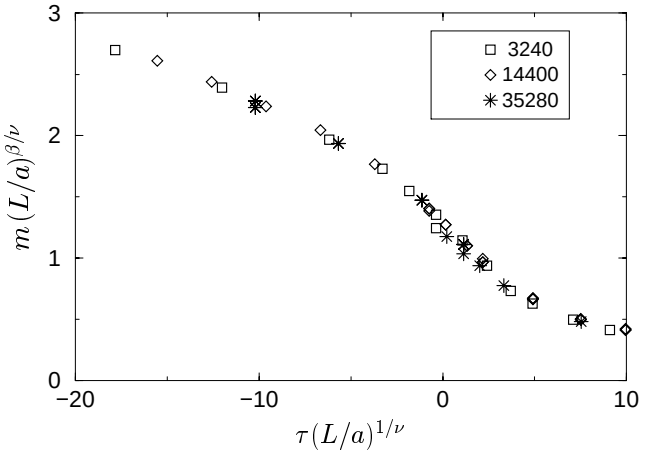

Fig. 15. Finite size scaling plot of the total average order parameter m for the composition $x = 0.73$, with $T_{\rm N} = 50.0(2)$ K and critical exponents, $\nu = 0.70(2)$ and $\beta = 0.35(2)$.

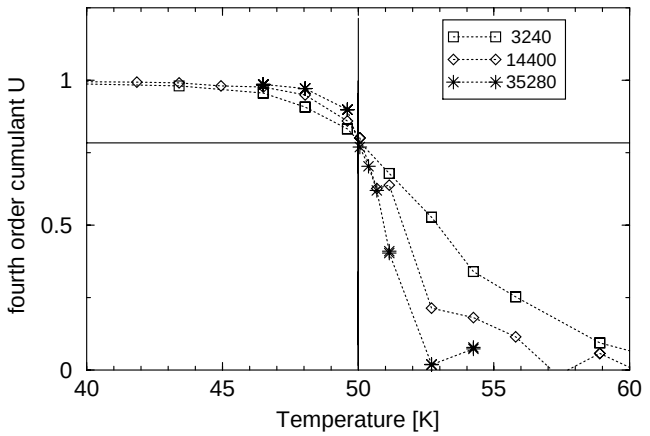

Fig. 14. Fourth order cumulant of the total order parameter m plotted *vs.* temperature for three different system sizes of models with the composition $x = 0.73$. The crossing determines $T_{\rm N} = 50.0(2)$ K and $\tilde{\rm U}^* = 0.78(2)$.

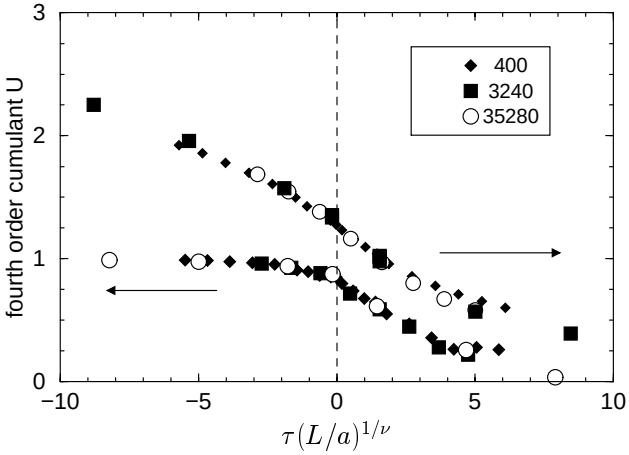

Fig. 16. Finite size scaling plots of the total order parameter m and the fourth order cumulant U for the model of GdS yield $T_{\rm N} = 61.3(3)$ K and critical exponents, $\nu = 0.71(2)$ and $\beta = 0.33(2)$.

Next we discuss our Monte Carlo results for the models of the pure system GdS. Again, the Néel-temperature has been determined from the cumulant crossing method, with $T_{\rm N} = 61.3(3)$ K. The best common scaling behaviour for the order parameter and the fourth order cumulant is found using similar values of the critical exponents, $\nu = 0.71(2)$ and $\beta = 0.33(2)$, see Figure 16.

Considering the critical behaviour all data remain consistent with $\beta = 0.35(2)$ and $\nu = 0.70(2)$. These results are still very close to the values for the Heisenberg model, $\beta = 0.367$ and $\nu = 0.707(3)$ [31], while MF theory predicts $\beta = \nu = 1/2$. Clearly, an attempt to use MF-exponents for scaling fails, as illustrated in Figure 17. Hence, no crossover to a MF regime is seen in the MCS.

One may note that in these models of $Gd_xEu_{1-x}S$ the observed changes in $T_{\rm N}$ with composition are not well reproduced, see Table 6, which indicates deficiencies of our still very simplified interaction model. Recall, in these MCS the interaction model is not altered with composition. However, a mere rescaling of the interactions with respect to $T_{\rm N}$ will not change the discussed critical properties.

Table 6. Néel-temperatures of $Gd_xEu_{1-x}S$. Comparison between measurements and Monte Carlo results obtained with the interaction model of Table 5.

	$x = 1$	$x = 0.8$	$x = 0.73$
experiment	57.72(3) K	53.5(5) K	36.4(5) K
MCS	61.3(3) K	53.3(3) K	50.0(2) K

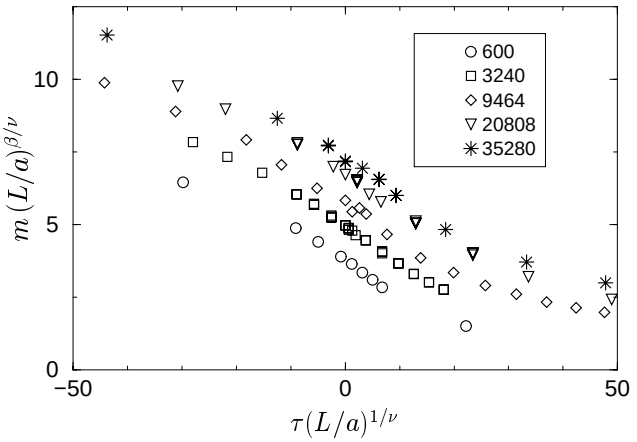

Fig. 17. Finite size scaling plot of the total average order parameter m for the composition $x = 0.8$, based on $T_N = 53.3$ K and mean-field critical exponents, $\nu = 1/2$ and $\beta = 1/2$, is clearly inadequate.

6 Discussion

Since we discussed the methodology of XRES in our former paper on pure GdS [16], we will mainly focus on the magnetic behaviour of the $Gd_xEu_{1-x}S$ mixed crystals in this discussion.

As it was discussed in detail in [16], the resonance line shape as a function of energy remains asymmetric after the absorption correction. The effect was explained with an interference of resonance exchange scattering and non-resonant magnetic scattering. With this model we were able to satisfactorily reproduce the line shape of the energy dependencies.

The values for the energy level width and the branching ratio determined with XRES are compatible with values and findings discussed in detail in [16]. The branching ratios between the resonance enhancements at the europium-L_{II}- and -L_{III}-edges are comparable to the ones at the gadolinium L-edges, but the resonance enhancements at the gadolinium-edges are about a factor five larger than at the europium-edges. To explain these findings, we have to discuss the electronic structure of $Gd_xEu_{1-x}S$ alloys [32–34]. According to [33], the $4f^7$ levels lie about 1 eV and 7 eV below the Fermi level for EuS and GdS, respectively. The $5d$ band consists of the e_g and t_{2g} subbands, has a total width of about 4 eV and a lower band edge about 1 eV above and below the Fermi level for EuS and GdS, respectively. Consequently, the europium ions in EuS are divalent and the compound is an insulator, while GdS is a metal due to the partially filled $5d$ conduction band. If Gd is doped into EuS, an impurity band forms some 10 meV below the Fermi level. At higher Gd concentrations, the impurity band merges into the conduction band of EuS. It is assumed that in an ionic picture, Eu remains divalent throughout the whole series, whereas Gd remains trivalent. This assumption is supported by the shape of the absorption edges, (see Fig. 2), which gives no indication for Eu^{3+} ions. The fact, that $Gd^{3+}$and Eu^{2+}have the same electronic ground state $^8S_{7/2}$ naturally explains the comparable branching ratios for the two elements. Apparently it cannot explain the smaller resonance enhancement at the Eu edges. We also can rule out the assumption that the europium ions do not reach a saturation magnetisation close to 7 μB, as was demonstrated by a comparison of the temperature dependence of the reduced sublattice magnetisation measured with XRES and neutron scattering. As was shown with a polarisation analysis of XRES, only electric dipole transitions $2p_{\frac{1}{2}} \rightarrow 5d$ or $2p_{\frac{3}{2}} \rightarrow 5d$ contribute significantly to the resonance enhancement at the L_{II}- and L_{III}-edges, respectively [16]. Two reasons for the different size of the resonance enhancement, despite the ions having the same electronic ground state, can be given. First, we may speculate that because the Gd^{3+}-ions are trivalent and the Eu^{2+}-ions are bivalent, the probability density of the electrons in the $5d$ valence band is larger close to the Gd^{3+}-ions (screening effect) and this leads to a larger resonance enhancement at the gadolinium-edges. Second, the Gd^{3+}-ion is significantly smaller as compared to the Eu^{2+}-ion, thus giving rise to different radial transition matrix elements.

After this discussion of XRES we now turn to the magnetic properties of the $Gd_xEu_{1-x}S$ mixed crystals. Both magnetic species, the gadolinium- and the europium-ions, participate in the antiferromagnetic order of type II for samples with a high gadolinium content. We could not detect any magnetic signal at positions in reciprocal space not corresponding to the antiferromagnetic order of type II neither with XRES nor with magnetic neutron scattering.

Our element-specific investigation of the temperature dependence of the reduced sublattice magnetisation revealed a different behaviour of the two magnetic species. The behaviour of the Gd^{3+}-ions in the two investigated samples $Gd_{0.8}Eu_{0.2}S$ and $Gd_{0.73}Eu_{0.27}S$ can be described by a simple mean-field curve for $S = \frac{7}{2}$ as is the case for pure GdS [16]. The temperature dependence of the sublattice magnetisation of the Eu^{2+}-ions differs significantly from mean-field. The temperature dependence of the reduced sublattice magnetisation is nearly linear over a wide temperature range. We were able to describe the temperature dependence with a simple model, which only takes nearest neighbour interactions on a simple cubic lattice into account. It shows that the deviations from the mean-field behaviour are due to frustration effects. These are caused by a competition between the ferromagnetic interactions of the europium-ions and an antiferromagnetic interactions of the gadolinium-ions, which cannot be satisfied simultaneously. Our MCS essentially confirm the frustration effects described by the mean-field model. Contrary to the mean-field model these simulations are performed on the complete cation sublattice and include the additional frustration effects between nearest neighbours that leads to the high degeneracy of the AF-II ground state. The results of MCS indicate that the ground state of the mixed systems $Gd_{0.8}Eu_{0.2}S$ and $Gd_{0.73}Eu_{0.27}S$ is not completely ordered.

Furthermore, we have found in the MCS an interesting effect of the ferromagnetic impurities on the coupling between order of the different simple cubic sublattices. In the pure system corresponding to GdS a collinear AF-II-structure was found in the simulations, which shows that thermal fluctuations lift the degeneracy of the ground states [35]. On the other hand the ferromagnetic impurities induce rather complex canted ordered states of the AF-II-structure. A similar situation has been analysed previously [36]. In a simpler model of non-magnetic impurities in a frustrated vector antiferromagnet (XY-model on a square lattice) the dilution induced perpendicular canted ordering or "anticollinear" ordering. In the present study ordered states with different canting angles changing with the dilution were found in the simulations at low temperatures indicating that in general the phase diagram is even richer than expected. Dipolar interactions have been neglected in the present study. According to [27] dipolar anisotropy is not able to restrict the order from the 8 sublattice to the 2-sublattice structure, while magnetostriction can have this effect, and therefore, it may also suppress the existence of possible canted ordered states in mixed frustrated magnetic systems. One might argue that the somewhat deliberate choice of this simplified interaction model may cause the discrepancies to the experimental observation. Of course, a better quantitative agreement with respect to transition temperatures, for instance, can be achieved by modified and more complex interaction models. However, a quantitative fit of the phase diagram is not the purpose of the MCS and in particular, this is not a unique determination that guarantees to obtain more realistic interactions. In principle, a better approach could be using the *inverse* Monte Carlo method to determine effective pair-exchange interactions [37] from measured short-range order spin correlations. However, ferromagnetic correlations that are likely for Eu-pairs cannot be separated from the intense charge-term Bragg scattering.

An investigation of the critical behaviour revealed critical exponents of $\beta_{\mathrm{Gd}} = 0.45(1)$ and $\beta_{\mathrm{Gd}} = 0.47(2)$ for the $Gd_{0.8}Eu_{0.2}S$- and $Gd_{0.73}Eu_{0.27}S$-samples, respectively. These values are close to the critical exponent $\beta = 0.5$ of the mean-field solution. They differ significantly from the Heisenberg-value $\beta = 0.378(20)$ which was observed for pure GdS [16]. We performed MCS to investigate possible changes of the critical exponents with Eu-content. Critical exponents ν and β are obtained from a finite size scaling analysis with values close to the theoretical Heisenberg values for all considered compositions. While the element-specific order parameters are distinctly different, in the MCS the critical behaviour of the specific elements is still described by the same critical exponents. There have been no detailed theoretical studies of the critical behaviour for mixed magnetic crystals [38]. One may speculate that, rather than frustration effects, possible long-range interactions induced by europium defects might be responsible for the experimental observation. For a dilution series, a change of the values of the critical exponents was predicted when the critical exponent of the specific heat of the undiluted system is positive [39]. With specific heat measurements a critical exponent $\alpha = 0.332(3)$ was determined for GdS [25] and for a dilution series, we could indeed expect a change of the critical exponents.

We now turn to the short-range ordered sample. In comparison to the $Gd_{0.73}Eu_{0.27}S$-sample, a small increase of the europium-concentration leads to a breakdown of the long-range antiferromagnetic order as observed for the $Gd_{0.67}Eu_{0.33}S$-sample. In the approach of our simple model described in Section 4, the increase of the europium-concentration leads to larger europium-clusters. In these clusters the ferromagnetic coupling dominates. This leads to a breakdown of the antiferromagnetic long-range order in the $Gd_{0.67}Eu_{0.33}S$- and $Gd_{0.6}Eu_{0.4}S$-samples. For the $Gd_{0.67}Eu_{0.33}S$-sample a short-range antiferromagnetic order with correlation lengths about some 10 Å was observed. The system disintegrates into an antiferromagnetically correlated gadolinium subsystem and ferromagnetically correlated europium subsystem. The Eu^{2+}-ions no longer take part in the antiferromagnetic order of the gadolinium subsystem.

7 Summary and conclusions

We have investigated the magnetic behaviour of $Gd_xEu_{1-x}S$ mixed crystals. XRES has been proven to be a versatile tool to determine element-specifically the properties of highly frustrated systems. We were able to observe the development of the spin glass state on a microscopic scale. In the gadolinium rich samples $Gd_{0.8}Eu_{0.2}S$ and $Gd_{0.73}Eu_{0.27}S$ the europium-ions exhibit an antiferromagnetic order. Frustration effects lead to a deviation of the reduced sublattice magnetisation of the europium-ions from the Brillouin-function with spin $S = \frac{7}{2}$. This is due to a ferromagnetic coupling in europium-clusters with two or more ions, as was demonstrated with a model calculation and MCS. The results of the XRES measurements were confirmed with magnetic neutron scattering. With further increasing europium concentration the europium-clusters become larger and the ferromagnetic coupling inside the clusters dominates. This leads to a breakdown of the long-range antiferromagnetic order as it was observed for the $Gd_{0.67}Eu_{0.33}S$- and $Gd_{0.6}Eu_{0.4}S$-samples.

In addition, the MCS revealed the possibility of canted ordered AF-II structures induced by frustration effects between nearest neighbours due to the ferromagnetic impurities.

For the first time it was possible to observe the element-specific short-range antiferromagnetic order in a spin glass state with XRES and to interpret this observation as a disintegration of the system into an antiferromagnetically correlated gadolinium- and a ferromagnetically correlated europium-subsystem.

We want to thank Mrs. Cornelisen, University of Hamburg, for performing the microprobe analysis. This work was supported by the Bundesministerium für Bildung und Forschung under contract number 03-BR4DES-2.

Appendix A: Mean-field treatment of the frustration in $Gd_xEu_{1-x}S$

In this appendix we describe the influence of the frustration effects due to ferromagnetic impurities on the antiferromagnetic structure within the mean-field approximation.

The Gd^{3+}- and Eu^{2+}-ions possess a spherically symmetric ground state with spin $S = \frac{7}{2}$. The interaction between the magnetic ions can therefore be described by a Heisenberg-Hamiltonian:

$$\mathcal{H} = -\sum_{i,j} J_{ij} \boldsymbol{S}_i \boldsymbol{S}_j. \tag{13}$$

To describe the stochastical occupation of the lattice sites we define a bivalent function P_i:

$$P_i = \begin{cases} 1 & \text{if site } i \text{ is occupied by } Gd^{3+} \\ 0 & \text{if site } i \text{ is occupied by } Eu^{2+} \end{cases}. \tag{14}$$

For stochastically occupied sites and x representing the proportion of Gd^{3+}-ions in $Gd_xEu_{1-x}S$ it follows:

$$\langle P_i \rangle = \frac{1}{N} \sum_i P_i = x. \tag{15}$$

The magnetic ions in $Gd_xEu_{1-x}S$ occupy the sites of a *fcc*-lattice in which the antiferromagnetic nearest neighbour interaction is highly frustrated and next nearest neighbour interactions have to be considered. Moreover, in the metallic phase a RKKY-interaction is present. Therefore in a realistic model for $Gd_xEu_{1-x}S$ the amount of parameters will be high and the main physical effect might be hidden. In order to avoid these complications our model calculation will be carried out for a simple cubic lattice with nearest neighbour interactions only. Even such a simplified model should show the modification of the temperature dependence of the sublattice magnetisation caused by frustration effects.

Using J_{GG}, $J_{EG} = J_{GE}$ and J_{EE} for the nearest neighbour interaction between Gd-Gd-, Gd-Eu- and Eu-Eu-pairs and defining $Q_i \equiv 1 - P_i$ we obtain the Hamiltonian:

$$\begin{aligned} \mathcal{H} = &-\sum_{i,j} J_{GG} P_i P_j \boldsymbol{S}_i \cdot \boldsymbol{S}_j - \sum_{i,j} J_{EE} Q_i Q_j \boldsymbol{S}_i \cdot \boldsymbol{S}_j \\ &- \sum_{i,j} J_{EG} P_i Q_j \boldsymbol{S}_i \cdot \boldsymbol{S}_j - \sum_{i,j} J_{EG} Q_i P_j \boldsymbol{S}_i \cdot \boldsymbol{S}_j. \end{aligned} \tag{16}$$

The transition temperatures of GdS and EuS (EuS doped with 3% Gd) are comparable [10]. Therefore we conclude that the Eu^{2+}-ions participate in the antiferromagnetic ordering for large x and we assume that the absolute values of the coupling constants J_{GG} and J_{EE} are of the same size: $|J_{GG}| \approx |J_{EE}|$. The Néel-temperature of the $Gd_xEu_{1-x}S$-mixed-crystals for large x does not depend on x, while for a dilution series ($J_{EG} = 0$) we expect the Néel-temperature to drop linearly. Because the Eu^{2+}-ions participate in the antiferromagnetic ordering for large x we assume for simplicity that J_{GG} and J_{EG} are of the same order of magnitude $J_{GG} \approx J_{EG} < 0$. Hence we can write for the Hamiltonian:

Table 7. Probability P_n of an Eu^{2+}-ion having n more Eu^{2+}-ions as nearest neighbours.

x	P_0	P_1	P_2	P_3	P_4	P_5
0.95	0.74	0.23	0.03			
0.90	0.53	0.35	0.10	0.01		
0.80	0.26	0.39	0.25	0.08	0.01	
0.73	0.15	0.34	0.31	0.15	0.04	0.01

$$\begin{aligned} \mathcal{H} = &-\sum_{i,j} \boldsymbol{S}_i \cdot \boldsymbol{S}_j \{J_{GG} P_i P_j + J_{EG} P_i Q_j + J_{EG} Q_i P_j \\ &+ J_{GG} Q_i Q_j\} - \sum_{i,j} \boldsymbol{S}_i \cdot \boldsymbol{S}_j Q_i Q_j (J_{EE} - J_{GG}) \\ \equiv &\, \mathcal{H}' + \Delta\mathcal{H} \end{aligned} \tag{17}$$

$\mathcal{H}'$ is the Hamiltonian of a system of Gd^{3+}-ions with single Eu^{2+}-ions, while $\Delta\mathcal{H}$ describes the effect of nearest neighbour Eu^{2+}-pairs. For small europium concentrations, we regard $\Delta\mathcal{H}$ as a small perturbation because it depends on the square of the Eu-concentration.

In our experiment we observed Bragg-scattering which averages over all possible realizations of disorder. The aim of this model calculation is to determine the expectation value $\langle \boldsymbol{S}_i \rangle$. Since the fluctuations $\Delta J = J_{GG} - J_{EG}$ are small, $\mathcal{H}'$ can be treated as spatially independent:

$$\begin{aligned} \mathcal{H}' &= -\sum_{i,j} \boldsymbol{S}_i \cdot \boldsymbol{S}_j \left\{J_{GG} - 2x\Delta J + 2x^2 \Delta J\right\} \\ &\equiv -\sum_{i,j} J' \boldsymbol{S}_i \cdot \boldsymbol{S}_j. \end{aligned} \tag{18}$$

For small ΔJ and x close to 1, J' changes nearly linearly with x. In equation (18), $\mathcal{H}'$ is again a well known Heisenberg Hamiltonian. In the mean-field approximation the expectation value can be determined:

$$\langle \boldsymbol{S}_i \rangle = \widehat{\boldsymbol{e}}\, v_i\, M(T). \tag{19}$$

The unit vector $\widehat{\boldsymbol{e}}$ determines the direction of the spins which are assumed to be collinear. v_i contains the sign of the spin for each site i and $M(T)$ represents the mean-field approximation of the temperature dependence of the sublattice magnetisation. The sublattice magnetisation of the majority ions $Gd^{3+}$and of isolated Eu^{2+}-ions will show the mean-field behaviour, but it has to be recognised that a spin moment belongs with the probability x to the Gd-subsystem. Next we consider the effect of the ferromagnetic Eu-Eu-interaction in europium nearest neighbour clusters, which is described by the term $\Delta\mathcal{H}$.

In a simple cubic lattice each site has six nearest neighbours. The probability that a lattice site is occupied by a Eu^{2+}-ion is $1 - x$. The probability for $0 \leq n \leq 6$ more Eu^{2+}-ions as nearest neighbours follows from the

Binomial-distribution. In Table 7 the probability P_n for a single Eu^{2+}-ion having n more Eu^{2+}-ions as nearest neighbours are listed for some compositions x.

For $x \to 1$, isolated Eu^{2+}-ions and Eu^{2+}-pairs dominate and we can neglect Eu^{2+}-clusters with more than two ions.

For Eu^{2+}-pairs the frustration effects, which are due to the exchange interactions of adjacent Eu^{2+}-ions, $\Delta\mathcal{H}$ has to be considered explicitly. If $\Delta\mathcal{H}$ is regarded as a perturbation of $\mathcal{H}'$, the energy eigenvalues can be calculated in first order approximation as the expectation value of the perturbation operator $\Delta\mathcal{H}$ with the wave functions of the undisturbed system. Consequently we use the mean-field approximation to describe the influence of the surrounding Gd^{3+}-ions on the Eu-pairs. This treatment, which was motivated by the perturbation theory, neglects the retroaction of the Eu^{2+}-pairs on the surrounding atoms. It follows from above for the Hamiltonian of a Eu^{2+}-pair in an antiferromagnetic molecular field:

$$\mathcal{H}_p = -2J\boldsymbol{S}_1 \cdot \boldsymbol{S}_2 - g\mu_\mathrm{B}(H_1\boldsymbol{S}_1^z + H_2\boldsymbol{S}_2^z). \qquad (20)$$

For simplicity we write J for J_EE, g is the Landé-factor, μ_B the Bohr-Magneton and H_1 and H_2 describe the molecular field of the surrounding Gd^{3+}-ions. If we use the eigenfunctions of the Heisenberg system as basis, $\mathcal{H}_p$ can be written as a matrix. With $\boldsymbol{S}' = \boldsymbol{S}_1 + \boldsymbol{S}_2$ as overall spin operator and M' as magnetic quantum number we get 64 eigenfunctions $|S'M'\rangle$ for an $S = \frac{7}{2}$ system and a 64×64 matrix $\langle S'M'|\mathcal{H}_p|S''M''\rangle$. The Heisenberg term $-2J\boldsymbol{S}_1 \cdot \boldsymbol{S}_2$ contributes only to the diagonal elements of the matrix. With the identity

$$\boldsymbol{S'}^2 = \boldsymbol{S}_1^2 + \boldsymbol{S}_2^2 + 2\boldsymbol{S}_1 \cdot \boldsymbol{S}_2 \qquad (21)$$

we get the following matrix elements from the Heisenberg term:

$$\langle S'M'| - 2J\boldsymbol{S}_1 \cdot \boldsymbol{S}_2|S''M''\rangle = \delta_{S''S'}\delta_{M''M'} \times \left[J\left(2S(S+1) - S'(S'+1)\right)\right]. \qquad (22)$$

To determine the matrix elements of the Zeemann term, we construct the wave function using the Clebsch-Gordan-coefficients $\langle Sm_1; Sm_2|S'M'\rangle$ and the product wave functions of the single spins $|Sm_1; Sm_2\rangle$:

$$|S'M'\rangle = \sum_{m_1=-S}^{+S}\sum_{m_2=-S}^{+S} |Sm_1; Sm_2\rangle\langle Sm_1; Sm_2|S'M'\rangle \cdot \qquad (23)$$

It follows for the matrix elements of the Zeemann term:

$$\begin{aligned}\langle S'M'| &- g\mu_\mathrm{B}(H_1\boldsymbol{S}_1^z + H_2\boldsymbol{S}_2^z)|S''M''\rangle \\ &= \sum_{m_1=-S}^{+S}\sum_{m_2=-S}^{+S}\sum_{m_3=-S}^{+S}\sum_{m_4=-S}^{+S} \langle S''M''|Sm_3; Sm_4\rangle \\ &\quad\times\langle Sm_3; Sm_4| - g\mu_\mathrm{B}(H_1\boldsymbol{S}_1^z + H_2\boldsymbol{S}_2^z)|Sm_2; Sm_1\rangle \\ &\quad\times\langle Sm_2; Sm_1|S'M'\rangle \\ &= -g\mu_\mathrm{B}\sum_{m_1=-S}^{+S}\sum_{m_2=-S}^{+S} \langle S''M''|Sm_2; Sm_1\rangle \\ &\quad(H_1m_1 + H_2m_2)\langle Sm_2; Sm_1|S'M'\rangle \cdot \end{aligned} \qquad (24)$$

The Clebsch-Gordan-coefficients are not equal to zero for $m_1 + m_2 = M' = M''$. Therefore the Zeemann term only contributes to matrix elements with $M' = M''$. If we use $m_1 = m$ and $m_2 = M' - m$, we get for the matrix elements of $\mathcal{H}_p$:

$$\begin{aligned}&\langle S''M''|\mathcal{H}_p|S'M'\rangle = \\ &\quad\delta_{S''S'}\delta_{M''M'}\left[J\left(2S(S+1) - S'(S'+1)\right)\right] \\ &\quad+\delta_{M''M'}\sum_m\left[-g\mu_\mathrm{B}(H_1m + H_2(M'-m))\right] \\ &\times\langle S(M'-m); Sm|S'M'\rangle \cdot \langle S(M'-m); Sm|S''M'\rangle \cdot \end{aligned} \qquad (25)$$

We sum over all indices m with $-S \le m \le +S$ and $-S \le M' - m \le +S$. The eigenvalues $E_{S'M'}$ and eigenvectors $|i\rangle$ can be evaluated numerically. With the help of the partition function

$$Z = \sum_{S'=0}^{2S}\sum_{M'=-S'}^{S'} \mathrm{e}^{-E_{S'M'}/k_\mathrm{B}T} \qquad (26)$$

it is possible to calculate the expectation value of the z component of the spins of the two Eu^{2+}-ions:

$$\langle \boldsymbol{S}_1^z\rangle = \frac{1}{Z}\mathrm{Tr}\left[\boldsymbol{S}_1^z\mathrm{e}^{-\mathcal{H}_p/k_\mathrm{B}T}\right] \cdot \qquad (27)$$

To be able to form the trace in equation (27), the representation of the operator $\boldsymbol{S}_1^z$ in the standardised base of the eigenvectors $|i\rangle$ is necessary:

$$\langle i|\boldsymbol{S}_1^z|i\rangle = \sum_{S'M'}\sum_{S''M''}\langle i|S'M'\rangle\langle S'M'|\boldsymbol{S}_1^z|S''M''\rangle\langle S''M''|i\rangle \cdot \qquad (28)$$

Analogous to the approach in the representation of the Zeemann term, which leads to equation (25), we get for the matrix elements of the z-component of the spin operator:

$$\begin{aligned}\langle S'M'|\boldsymbol{S}_1^z|S''M''\rangle = \delta_{M'M''}&\sum_{m_1=-S}^{+S}\sum_{m_2=-S}^{+S} \\ &\langle S'M'|Sm_2; Sm_1\rangle m_1\langle Sm_2; Sm_1|S''M'\rangle \cdot \end{aligned} \qquad (29)$$

From equation (28, 29) it follows:

$$\begin{aligned}\langle i|\boldsymbol{S}_1^z|i\rangle = &\sum_{S'M'}\sum_{S''}\sum_m m\langle i|S'M'\rangle \cdot \langle S''M'|i\rangle \\ &\times\langle S'M'|S(M'-m); Sm\rangle \cdot \langle S(M'-m); Sm|S''M'\rangle \cdot \end{aligned} \qquad (30)$$

The Clebsch-Gordan-coefficients are well known and the coefficients $\langle i|S'M'\rangle$ can be obtained from the diagonalisation of the matrix. Therefore it is straightforward to calculate $\langle i|\boldsymbol{S}_1^z|i\rangle$ in (30) numerically and then obtain $\langle S_1^z\rangle$ from (27).

The numerical calculation of the expectation value $\langle \boldsymbol{S}_1^z\rangle$ was done with a Fortran 77 program. The Clebsch-Gordan-coefficients were calculated with the Racah-formula [40]. For the diagonalisation of the weakly occupied matrix in equation (25) and the determination of

the eigenvalues and eigenvectors special routines of the program package "Eispack" [41–43] were used.

To describe the sublattice magnetisation of the Eu^{2+}-ions we summed the expectation value of single Eu^{2+}-ions and Eu^{2+}-pairs (Eq. (27)) weighted with their relative occurance (see Tab. 7). Eu-cluster with more than two Eu^{2+}-ions were neglected.

References

1. D. Gibbs, D. Harshman, E. Isaacs, D. McWhan, D. Mills, C. Vettier, Phys. Rev. Lett. **61**, 1241 (1988).
2. E. Isaacs, D. McWhan, D. Siddons, J. Hastings, D. Gibbs, Phys. Rev. B **40**, 9336 (1989).
3. J. Bohr, D. Gibbs, K. Huang, Phys. Rev. B **42**, 4322 (1990).
4. D. Gibbs, J. Bohr, J. Axe, D. Moncton, K. D' Amico, Phys. Rev. B **34**, 8182 (1996).
5. C. Detlefs, A. Goldman, C. Stassis, P. Canfield, B. Cho, J. Hill, D. Gibbs, Phys. Rev. B **53**, 6355 (1996).
6. S. Langridge, G. Lander, N. Bernhoeft, A. Stunault, C. Vettier, G. Grübel, C. Sutter, F. de Bergevin, W. Nuttall, W. Stirling, K. Mattenberger, O. Vogt, Phys. Rev. B **55**, 6392 (1997).
7. J. Hill, C.C. Kao, D. McMorrow, Phys. Rev. B **55**, 8662 (1997).
8. D. Pengra, N. Thoft, M. Wulff, R. Feidenhans'l, J. Bohr, J. Cond. Matt. **6**, 2409 (1994).
9. A. Stunault, C. Vettier, F. de Bergevin, F. Maier, G. Grübel, R. Galéra, S. Palmer, J. Magn. Magn. Mat. **140–144**, 753 (1995).
10. A. Berton, J. Chaussy, J. Odin, R. Rammal, J. Souletie, J. Tholence, R. Tournier, J. Appl. Phys. **52**, 1763 (1981).
11. M. Blume, J. Appl. Phys. **57**, 3615 (1985).
12. M. Blume, D. Gibbs, Phys. Rev. B **37**, 1779 (1988).
13. J. Hannon, G. Trammel, M. Blume, D. Gibbs, Phys. Rev. Lett. **61**, 1245 (1988).
14. J. Luo, G. Trammell, J. Hannon, Phys. Rev. Lett. **71**, 287 (1993).
15. M. Blume, in *Resonant anomalous X-ray scattering*, edited by G. Materlik, C. Sparks, K. Fischer (Elsevier Science B.V., 1994), pp. 231–256.
16. T. Brückel, D. Hupfeld, J. Strempfer, W.A. Caliebe, K. Mattenberger, A. Stunnault, N. Bernhoeft, G. McIntyre, Eur. Phys. J. B **19**, 475 (2001).
17. D. Hupfeld, W. Schweika, J. Strempfer, K. Mattenberger, G.J. McIntyre, T. Brückel, Europhys. Lett. **49**, 92 (2000).
18. K. Mattenberger, L. Scherrer, O. Vogt, J. Cryst. Growth **67**, 467 (1984).
19. T. Brückel, R. Nowak, T. Köhler, U. Brüggmann, U. Maul, E. Pfützenreuter, V. Rilling, W. Prandl, J. Appl. Cryst. **29**, 686 (1996).
20. J. Voss, J. Electron Spectroscopy **84**, 29 (1997).
21. M. Lehmann, W. Kuhs, G. McIntyre, C. Wilkinson, J. Allibon, J. Appl. Cryst. **22**, 562 (1989).
22. J. Kirz, D.T. Attwood, B.L. Henke, M.R. Howells, K.D. Kennedy, K.J. Kim, J.B. Kortright, R.C. Perera, P. Pianetta, J.C. Riordan, J.H. Scofield, G.L. Stradling, A.C. Thompson, J.H. Underwood, D. Vaughan, G.P. Williams, H. Winick, *X-ray data booklet* (Lawrence Berkley Laboratory, Berkley, California, 1986).
23. D. Hupfeld, Dissertation, Universität Hamburg (1998), ISSN 1435-8085.
24. F. Hulliger, T. Siegrist, Z. Physik B **35**, 81 (1979).
25. U. Köbler, D. Hupfeld, W. Schnelle, K. Mattenberger, T. Brückel, J. Magn. Magn. Mater. **205**, 90 (1999).
26. W. Nolting, *Quantentheorie des Magnetismus Band 1 & 2* (B.G. Teubner, Stuttgart, 1986).
27. R. Nowotny, K. Binder, Z. Phys. B **77**, 287 (1989).
28. P. Bak, B. Lebech, Phys. Rev. Lett. **40**, 800 (1978).
29. K. Binder, D. Heermann, *The Monte Carlo Method in Statistical Physics. An Introduction* (Springer, 1988).
30. V. Privman, *Finite Size Scaling and the Numerical Simulation of Statistical Systems* (World Scientific, Singapore, 1990).
31. M.F. Collins, *Magnetic critical scattering* (Oxford University Press, Oxford, 1989).
32. T. Kasuya, A. Yanase, Rev. Mod. Phys. **40**, 684 (1968).
33. P. Wachter, Phys. Rep. **44**, 159 (1978).
34. G. Borstel, W. Borgiel, W. Nolting, Phys. Rev. B **36**, 5301 (1987).
35. T. Brückel, C. Paulsen, K. Hinrichs, W. Prandl, Z. Phys. B **97**, 391 (1995).
36. C.L. Henley, Phys. Rev. Lett. **62**, 2056 (1989).
37. W. Schweika, *Disordered Alloys, Diffuse Scattering and Monte carlo Simulation*, Vol. 141 (Springer Tracts in Modern Physics, Springer, Heidelberg, 1998).
38. W. Selke, L. Shchur, A. Talapov, Ann. Rev. Comput. Phys. **I**, 17 (1994).
39. A.B. Harris, J. Phys. C **7**, 1671 (1974).
40. A. Messiah, *Quantum Mechanics*, Vol. II (North-Holland publishing company, Amsterdam, 1975).
41. Program package eispack, `ftp://netlib.bell-labs.com/netlib/eispack.tar` (1983).
42. B. Smith, J. Boyle, J. Dongerra, B. Garbow, Y. Ikebe, V. Klema, C. Moler, *Matrix eigensystem routines – EISPACK guide, lecture notes in computer science*, Vol. 6 (Springer-Verlag, New York, Heidelberg, Berlin, 1976).
43. B. Garbow, J. Boyle, J. Dongerra, C. Moler, *Matrix eigensystem routines – EISPACK guide extension, lecture notes in computer science*, Vol. 51 (Springer-Verlag, New York, Heidelberg, Berlin, 1977).